PASJ: Publ. Astron. Soc. Japan , 1–??,

The Virgo High-Resolution CO Survey: VI. Gas Dynamics and Star Formation Along the Bar in NGC 4303

Jin KODA
California Institute of Technology, MS 105-24, Pasadena, CA 91125, USA;
and National Astronomical Observatory, Mitaka, Tokyo, 181-8588, Japan
koda@astro.caltech.edu
and
Yoshiaki SOFUE
Institute of Astronomy, University of Tokyo, Mitaka, Tokyo, 181-0016, Japan
sofue@ioa.s.u-tokyo.ac.jp

(Received 0 0; accepted 0 0)

Abstract

We present CO interferometer observations of the barred galaxy NGC 4303 (M61). This galaxy has a strong gas concentration at the central region and prominent offset ridges at the leading sides of the bar. Sharp velocity gradients are apparent across the ridges. The brightness temperature in the ridges is low, indicating the existence of unresolved molecular clouds. Star formation appears inactive in Hα image, but *HST* images show young stellar clusters with masses $10^{3-4}M_{\odot}$. Assuming the star formation efficiency 0.01-0.1, their parent molecular clouds should have had masses $10^{4-6}M_{\odot}$. Observed shear velocity gradient across the ridges is too small to break up the clouds, and therefore, the clouds survive after passing the offset ridges. We discuss a cloud orbit model in bar for understanding the gas distribution, dynamics, and star formation in NGC 4303. The model reproduces the narrow offset ridges and sharp velocity gradients across the ridges. In this model, no shock is associated with the offset ridges, which explains the inactive star formation along the ridges. We discuss cloud-cloud collision (and close interaction) as a possible triggering mechanism for star formation. The young stellar clusters in NGC 4303 are located predominantly at the leading sides of the offset ridges. Some of them are found far from the ridges, indicating their birth long after the parent clouds have passed the ridges. Cloud orbits are densely populated around the region where the clusters are found, indicating a high collisional frequency and star formation. Cloud-based dynamics is less dissipational than hydrodynamic models, and would change the timescales of gas dynamical evolution and gas fueling to central regions in barred galaxies.

Key words: galaxies:individual(NGC 4303) - galaxies:kinematics and dynamics - galaxies:ISM

1. Introduction

Despite numerous observational and theoretical studies, the nature of interstellar medium (ISM) in gas dynamics has remained unknown (Combes 1996). Dynamical response of the gas depends significantly on whether ISM is continuous hydrodynamic fluid or a set of discrete molecular clouds. The hydrodynamic fluid produces shock along spiral arm or bar in galaxies, while the molecular clouds could ballistically pass the spiral/bar structures without shock. Such difference must change not only the dynamical response of the gas (e.g. shock, dissipation), but also the evolution timescale (e.g. gas inflow) and star formation.

The Galactic ISM concentrates in discrete molecular clouds (Scoville & Sanders 1987), and favors the dynamics of slightly-collisional clouds. Individual molecular clouds are hardly resolved in external galaxies, however, there is a general belief that only continuous hydrodynamic models could reproduce narrow gas/dust lanes observed in barred galaxies, since hydrodynamic fluid easily produces narrow shock lines along bars. On the contrary, we demonstrate that a cloud-based gas dynamics model also reproduces the narrow gas distribution and associated gas kinematics in bars.

A clue to understanding gas dynamics could be found in the large-scale distribution of star forming regions and young stars. Star formation triggered by hydrodynamic shock would be localized on narrow shocked regions. Cloud-cloud interaction could potentially occur everywhere in galactic disks and cause star formation. We compare CO observations of the barred galaxy NGC 4303 (M61) to the cloud-based gas dynamics model, and investigate the distribution of young stellar clusters.

Figure 1 shows the B and Hα band images of NGC4303; most HII regions are associated with outer spiral arms, but almost no apparent Hα emission is found in the bar. Similar trends have been found in many other barred galaxies (Downes et al. 1996; Regan, Teuben & Vogel 1996; Garcia-Barreto et al. 1996; Sheth et al. 2000; Sheth et al. 2002). The absence of active star formation in bar is often attributed to strong shear velocity around the bar (Reynaud & Downes 1998). We, however, discuss that the shear velocity in NGC 4303 is too low to break

up dense molecular clouds.

NGC 4303 hosts remarkable central activity: nuclear secondary bar (Colina & Wada 2000), prominent UV emission around the secondary bar (Colina et al. 1997), and active galactic nucleus (AGN; Colina & Arribas 1999). It has been of interest in the context of starburst-AGN connection (Colina et al. 1997; Colina & Arribas 1999; Colina & Wada 2000; Jimenez-Bailon et al. 2003). Schinnerer et al. (2002) discussed the gas fueling toward the nucleus due to the secondary bar based on their CO data. Our focus, however, is on the gas dynamics and star formation around the offset ridges in the primary bar.

We describe the observations and data in §2, and results in §3. We introduce a cloud-orbit model in bar and show its ability to reproduce the observed CO distribution and velocity structure (§4). We discuss star formation along the bar using the cloud-based model (§5). Conclusions are summarized in §6. This paper is the sixth in a series on the Virgo CO survey at the Nobeyama Millimeter Array (Sofue et al. 2003a; Sofue et al. 2003b; Sofue et al. 2003c; Onodera et al. 2004; Nakanishi et al. 2005).

—— Figure 1 ——

—— Table 1 ——

2. Observational Data

2.1. NMA CO(1-0) Observations

We made aperture synthesis observations of the Virgo cluster galaxy NGC 4303 in the CO $J = 1 - 0$ line emission using the Nobeyama Millimeter Array (NMA). The observations were made between 1999 December and 2000 February for a single pointing center at (α_{1950}, δ_{1950}) = ($12^{\rm h}19^{\rm m}21^{\rm s}.6$, $+4^\circ45'3''.0$). Six 10 m telescopes provide the FWHP of about $65''$ at 115 GHz. We used three available array configurations (AB, C, and D configurations). Typical system noise temperature were about 400 K in single sideband. Digital spectro-correlators (Okumura et al. 2000) have two spectroscopic modes; we used the mode covering 512 MHz ($1331\,{\rm km\,s^{-1}}$) with the 2 MHz ($5.2\,{\rm km\,s^{-1}}$) resolution. We observed the quasar 3C273 every 20 minutes for gain and bandpass calibrations. The absolute flux of 3C273 was measured against URANUS and/or available flux-known quasars; it was 14.2Jy for December 1999, and 11.4Jy for January and February 2000. The uncertainties in the flux scale are about 20%.

Raw visibility data were calibrated for passband response and complex gain variation with the NRO/UVPROC-II package (Tsutumi, Morita & Umeyama 1997). The data were binned to 4 MHz resolution. Each channel data was deconvolved with the CLEAN procedure using the NRAO/AIPS package. We applied both natural and uniform weightings for the visibility data and obtained $2.4''$- and $1.3''$-resolution maps, respectively. We refer the $2.4''$-resolution map as "map". Parameters of the observation and data cubes are in Table 2 and 3, respectively.

—— Table 2 ——

—— Table 3 ——

Figure 2 shows zeroth- and first-moment maps, and synthesized beam map. Figure 3 and 4 show the velocity channel maps and position-velocity (PV) diagrams, respectively. Primary beam attenuation is not corrected for these maps. In the synthesized beam map (Figure 2), prominent sidelobes are running in the north-south direction and aligned with the observed emission distribution. These sidelobes made the deconvolution less obvious; we arranged restricted CLEAN boxes and checked that 2nd- and 3rd-order sidelobes are also reduced successfully in the deconvolution. We estimated the recovered flux by comparing our data with a single-dish observation at the FCRAO 14 m telescope (Kenney & Young 1988). Our map recovers 97% of the total flux in the central $45''$ (with the uncertainties of 20%) .

—— Figure 2 ——

—— Figure 3 ——

—— Figure 4 ——

2.2. Supplied Optical/Near-IR Data

We obtained optical and near-infrared images from the archives and literature through the NASA/IPAC Extragalactic Database (NED), i. e. the B-band image from the Digitized Sky Survey, Hα-image (Figure 1 & 5) from Koopmann, Kenney & Young (2001), and K-band image (Figure 5) from Moellenhoff & Heidt (2001). We also obtained *HST* images in the F450W and F814W-filters (P.I. Smartt) through the HST archive at the Canadian Astronomy Data Center (CADC). The F450W and F814W images are shown in Figure 6.

The astrometry of the B- and Hα-band images was determined using the USNO-A2.0 catalog (Zacharias et al. 2000). The K-band and *HST* images do not contain enough cataloged stars; we shift a central compact emission in each image on the dynamical center (§3.3). The centroids of compact sources across these images coincide with those in the lower-resolution B-band image. The uncertainties of the absolute position in each image is about $0.5''$.

—— Figure 5 ——

—— Figure 6 ——

3. Results

Figure 2 shows two remarkable features in the gas distribution: (1) central concentration within $r \sim 10''$ (780 pc, hereafter central disk), and (2) offset ridges extending from the central concentration out to $r \sim 30''$ (2.3 kpc). The gas is rotating clockwise in assuming trailing spiral arms. We obtain the parameters of the gas disk and discuss the two features.

3.1. Global CO Properties

Figure 7 shows the radial profile of CO integrated intensity $I_{\rm CO}{\rm d}V\cos(i)$ and cumulative flux $S_{\rm CO}$. Corrections

for primary beam response and inclination were applied. We adopted the position angle P.A. $= -45°$, inclination $i = 30°$ (see §3.2), and the CO-to-H_2 conversion factor $X_{\rm CO} = 1.8 \times 10^{20} {\rm cm}^{-2} [{\rm K\,km\,s}^{-1}]^{-1}$ (Dame, Hartmann & Thaddeus 2001). The surface density is almost constant $\sim 500 M_\odot\,{\rm pc}^{-2}$ from the center to $r \sim 4''$ (310 pc), and decreases exponentially with the scale length of $\sim 4.5''$ (350 pc). Total detected gas mass is $8.4 \times 10^8 M_\odot$ within the radius $13''$ (1 kpc), and is $1.0 \times 10^9 M_\odot$ within $30''$ (2.3 kpc).

—— Figure 7 ——

3.2. Central Concentration

The CO emission is concentrated in the central disk ($r < 10''$) in Figure 2. The velocity field resembles so-called "spider diagram". The gas is following almost pure circular rotation. Spiral arms are curling along the outer edge of the central disk (Figure 8). They are associated slight perturbations in the velocity field at the outer edges of the central disk. We obtain kinematic parameters from the velocity-field assuming pure circular rotation. Dynamical center, position angle, inclination, and recession velocity are determined using the AIPS/GAL package. Table 4 lists the results. Since the perturbations due to the spiral arms are small, the error due to the perturbations should be small. The derived parameters are consistent with the ones in previous studies (Colina & Arribas 1999; Schinnerer et al. 2002).

—— Figure 8 ——

3.3. Offset Ridges

Two gas ridges run out from the central disk in the north and south directions (Figure 2). Figure 5 (*left*) compares the gas distribution (greyscale; CO image) with the stellar bar (contours; K-band image). The two ridges are at the leading sides of the stellar bar. This type of ridge is referred to "offset ridges", and often found in barred galaxies (Ishizuki et al. 1990; Sakamoto et al. 1999; Sheth et al. 2002). The gas ridges coincide with dust lanes in Figure 6. There are gas concentrations at the outermost ends of the detected CO ridges (Figure 2), which coincide with the stellar bar ends. Such gas concentration is common in barred galaxies. Note that no primary beam correction has been applied to this map; the fluxes of these gas concentrations are about 2 times larger than the contour values in the figure.

Sharp velocity gradients exist across the offset ridges; in the channel maps (Figure 3), the southern CO ridge shifts east (toward left) as the velocity decreases, and the northern ridge shifts west (right) as the velocity increases. The isovelocity contours run along the offset ridges in the velocity field map (Figure 2). The velocity differences across the ridges $\sim 4''$ is about $\sim 20\,{\rm km\,s}^{-1}$ (i. e. three channels) in the projection on the sky.

Typical brightness temperature is $T_{\rm b} \sim 1$ K along the offset ridges (Figure 3). Assuming the excitation temperature $T_{\rm ex} = 10$ K for optically-thick molecular gas (Scoville & Sanders 1987) and cosmic microwave background temperature $T_{\rm CMB} = 3$ K, the area filling factor within the beam ($2.4'' \sim 200$ pc) is $f \sim 0.1$. Thus, unresolved clumpy structures, presumably molecular clouds, exist. Average gas surface density in the beam is typically $\Sigma_{\rm gas} = 150 M_\odot\,{\rm pc}^{-2}$. Therefore, the molecular clouds are dense, i. e. $\Sigma_{\rm gas}/f \sim 1000 M_\odot\,{\rm pc}^{-2}$. This is much denser than $170 M_\odot\,{\rm pc}^{-2}$ for the clouds in the Galactic disk (Solomon et al. 1987), but less dense than $2500 M_\odot\,{\rm pc}^{-2}$ for the clouds in the Galactic center (Oka et al. 2001).

3.4. Star Formation Around Offset Ridges

Evidence of star formation (SF) around the offset ridges is inferred in the *HST* images (Figure 6), although active SF is not apparent in the Hα image (Figure 5 *right*). The *HST* images show a few hundreds of small dots around the bar, each of which correspond to a young stellar cluster. Their luminosities indicate that the masses are $10^{3-4} M_\odot$. Assuming the extinction $A_V = 1$ mag and color excess 0.71 (Cardelli, Clayton & Mathis 1989), the typical color in F450W-F814W is as blue as -0.7 mag (AB magnitude), indicating their young ages $\lesssim 10^7$ yr (see Appendix 1). Because of the large scatter in color (± 0.5 mag), we could not recognize any systematic spatial variation of the color.

The clusters are distributed predominantly at the leading (downstream) side of the gas ridges, i. e. the east of the southern ridge and the west of the northern ridge. No obvious cluster is found at the opposite (upstream) side, which is especially remarkable for the southern ridge. Therefore, the SFs were initiated either during or after the passage of parent molecular cloud across the offset ridges. Some stellar clusters are found *far* from the gas ridges. The rotation timescale around the galaxy 10^8 yr is ten times longer than the cluster age $\lesssim 10^7$ yr. Thus, those clusters should have been formed not *on* the ridges, but *long after* the passage of the cloud across the ridges.

The conversion of molecular gas to stars in a molecular cloud is a very ineffective process in the Galaxy. Assuming the conversion efficiency 0.01-0.1 (Evans & Lada 1991; Lada 1992), the parent molecular clouds of the stellar clusters should have had the mass $10^{4-6} M_\odot$, which is typical for Galactic molecular clouds (Scoville & Sanders 1987).

3.5. Comparison with Other CO Maps

Three CO maps have been published from mm-wave interferometer observations, at the Owens Valley Radio Observatory (OVRO; Schinnerer et al. 2002), at the Nobeyama Millimeter Array (NMA; Sofue et al. 2003a, and this paper), and at the Berkeley-Illinois-Maryland Association (BIMA; Helfer et al. 2003).

The BIMA map has three times lower sensitivity ~ 47 mJy and resolution $\sim 6''$, but covers three times wider region $190''$. The map includes zero-spacing baselines (extended components) from single dish observations, and thus, is good for tracing the large scale distribution of molecular gas. In their map, significant CO emission is apparent along outer spiral arms. Their brightness are comparable between the offset ridges and spiral arms, though

star formation is more active in the arms (Figure 1).

The OVRO map has similar sensitivity $\sim 20\,\mathrm{mJy}$ and resolution $\sim 2''$ to our map. The CO distribution and velocity structure are consistent between the OVRO and NMA maps. The recovered flux in comparison with the single-dish data (Kenney & Young 1988), however, is 2 times higher in NMA than in OVRO. We compared the two data cubes[1] and found that the NMA flux is ~ 1.4 times larger in spectrum and ~ 2 times greater in integrated intensity. Perhaps, the first 1.4 comes from the absolute flux calibration. Both observations were made at almost the same time using the same calibrator 3C273. The 3C273 flux was $\sim 14\,\mathrm{Jy}$ in our measurement (for the smallest configuration), but was $\sim 10\,\mathrm{Jy}$ in a record at OVRO. The other 1.4 may come from deep negative sidelobes around strong emissions in the OVRO data; as a test, we swapped the negative flux values for zero, and found that the integrated intensities match well. Fortunately, this difference does not affect the discussions made in this paper and in Schinnerer et al. (2002).

4. Gas Dynamics in NGC 4303

We have shown the existence of molecular clouds in §3. We use a cloud-orbit model to interpret gas dynamics in NGC 4303. To derive stellar orbits in bar, the equations of motion for a test particle are solved in a bar potential (Contopoulos & Papayannopoulos 1980; Binney & Tremaine 1987). Wada (1994) included the damping force term "$-2\lambda\dot{R}$" in the equations of motion, i. e. the force negatively proportional to the velocity $\dot{R}$, and obtained the orbits of collisional gas clouds. This model has provided successful interpretations for observed barred and spiral galaxies (Sakamoto, Baker & Scoville 2000; Koda et al. 2002a; Onodera et al. 2004). Figure 9, 10, and 11 show the model gas orbits, density and velocity field maps, and position-velocity diagrams. The gas and bar are rotating clockwise. The model is scalable; it fits to NGC 4303 when the units are 300 pc in length and $160\,\mathrm{km\,s^{-1}}$ in velocity. The pattern speed and bar radius (corotation radius) are scaled to $53\,\mathrm{km\,s^{-1}\,kpc^{-1}}$ and 3 kpc, respectively, which is consistent with the bar radius in Figure 1.

—— Figure 9 ——

4.1. Offset Ridges and Central Spirals

Figure 10 shows the projection of gas orbits with the position angle $-45°$ and inclination $30°$ (Table 4). The stellar bar runs vertically. The density map (*middle*) reproduces the observed offset ridges and central spiral arms in Figure 2. To calculate the density, we used the timescale of passage along orbit as a weighting function. The offset ridges and central spiral arms appear dense for two reasons: (1) the gas orbits are crowded at the leading side of the bar, and (2) passing the apocenter of an orbit takes longer than passing the pericenter.

[1] OVRO data cube was kindly provided by Eva Schinnerer.

There is a common belief that the offset ridges are produced by hydrodynamic shock; the tangential orbital velocity of the gas is damped by the shock and the gas falls toward the galactic center along the offset ridges. The orbit model, however, proved that *no shock is required to form the dense and narrow offset ridges.* In fact, the sharp turns are apparent in the *rotating* frame with the bar (Figure 9 *left*), but disappear in the rest frame (*right*). This fact is particularly important when the orbits of young stars born recently in molecular clouds are discussed. We note that this argument does not exclude a possibility of shock as a secondary effect.

—— Figure 10 ——

The velocity field (Figure 10 *right*) is consistent with the observations (Figure 2 *middle*). The major axes of elongated gas orbits are aligned with that of the galaxy at the central disk, and therefore, the isovelocity contours are similar to those of pure circular rotation (spider diagram). Slight deviations from pure circular rotation are apparent along the spiral arms on the central disk; we found similar deviations in the observed velocity field (Figure 2 *middle*). At the outer part, the isovelocity contours run along the offset ridges as found in the observations. The contours parallel to the offset ridges indicate abrupt velocity changes across the ridges, although no shock is associated.

—— Figure 11 ——

Figure 11 shows position-velocity (PV) diagrams with three different position angles (PA). The diagram with $\mathrm{PA} = -45°$ corresponds to NGC 4303 and is similar to the observed one. The model reproduced the observations in space (maps) and velocity (PV diagram), indicating that the orbit model represents the gas motions in NGC 4303. The other two diagrams, i.e. $\mathrm{PA} = 0°$ and $-90°$, are the projections from the edge-on and pole-on directions of the bar, respectively. The same gas distribution shows quite different patterns; our determination of the PA and inclination in §3.2 were suitable for NGC 4303.

4.2. Cloud-cloud Collision as Damping Force

The damping force term "$-2\lambda\dot{R}$" provides the damping timescale $t_{\mathrm{damp}} = 1/\lambda$ in which random motions decay. For the above model, we set $\Lambda \equiv \lambda/\kappa_0 = 0.1$ as in previous studies (Wada 1994; Sakamoto, Baker & Scoville 2000). The orbits are insensitive to the change of Λ by a factor of a few (Wada 1994). We discuss its physical cause in an order of magnitude. Assuming a constant rotation velocity $V = 160\,\mathrm{km\,s^{-1}}$ at the radius 1 kpc as for NGC 4303, the epicyclic frequency becomes $\kappa_0 \sim 200\,\mathrm{km\,s^{-1}\,kpc^{-1}}$. The damping timescale is then $t_{\mathrm{damp}} = 1/\Lambda\kappa_0 \sim 5 \times 10^7\,\mathrm{yr}$ for $\Lambda = 0.1$.

We have shown the presence of dense molecular clouds in NGC 4303 (§3.3). The above timescale is close to the collisional timescale of clouds calculated as follows. NGC 4303 has the gas mass $10^8 M_\odot$ between the radii of $1-2\,\mathrm{kpc}$ (Figure 7). Assuming the cloud mass $M_{\mathrm{MC}} = 10^5 M_\odot$ and diameter $D = 20\,\mathrm{pc}$, the surface number density of molecular clouds is $N_{\mathrm{MC}} = 100\,\mathrm{kpc^{-2}}$. If the cloud-cloud ve-

locity dispersion is $\sigma = 10\,\mathrm{km\,s^{-1}}$ and the galactic molecular disk is thin (2-D) at the central region, the collisional timescale between molecular clouds becomes $t_{col} = 1/N_{\rm MC} D\sigma \sim 4\times10^7\,\mathrm{yr}$. Close encounter would occur in slightly shorter timescale but in the order of 10^7 yr. These are close to the damping timescale for $\Lambda \sim 0.1$. The cloud collision could be the cause of the damping force.

Ram pressure from ambient gas is negligible. Using the density of the ambient gas ρ, relative velocity between a cloud and the ambient gas v, cloud cross section A, and mass $M_{\rm MC}$, the acceleration on the cloud is $a_{\rm ram} = \rho v^2 A/M_{\rm MC}$. The velocity difference would decay in $t_{\rm ram} = v/a_{\rm ram}$. If the ambient gas is atomic hydrogen with the density $1\,\mathrm{cm^{-3}}$ and the velocity $v = 10\,\mathrm{km\,s^{-1}}$, $t_{\rm ram} \sim 10^9\,\mathrm{yr}$, which is much longer than $t_{\rm col}$.

4.3. Shear Velocity and Survival of Molecular Clouds

Downes et al. (1996) discussed that molecular clouds might be destroyed by strong shear around offset ridges. Assuming that the shapes and orientations of the gas orbits in Figure 10 *left* are all correct, molecular clouds have only the velocity components tangential to our line-of-sight before the ridges, and only the line-of-sight velocity components after the ridges. The velocity difference across the ridges is then $\sim 40\,\mathrm{km\,s^{-1}}$ from the observed velocity difference $20\,\mathrm{km\,s^{-1}}$ and inclination 30°. The width of the ridge is $\sim 300\,\mathrm{pc}$ ($\sim 4''$), and thus, the velocity gradient (shear) is about $0.13\,\mathrm{km\,s^{-1}\,pc^{-1}}$.

The surface density of a molecular cloud in NGC 4303 is about $\Sigma_{\rm MC} = 1000 M_\odot\,\mathrm{pc^{-2}}$ (§3.3). Assuming the cloud radius $R = 10\,\mathrm{pc}$, the escape velocity from the cloud, i. e. $v_{\rm esc} = (2\pi G \Sigma_{\rm MC} R)^{1/2}$, is $16\,\mathrm{km\,s^{-1}}$. Thus, a sharp velocity gradient $1.6\,\mathrm{km\,s^{-1}\,pc^{-1}}$ is necessary to destroy the molecular cloud. This is an order of magnitude above the observed shear velocity gradient in NGC 4303. Even for some molecular clouds with lower surface densities $100 M_\odot\,\mathrm{pc^{-2}}$ (typical for the Galactic molecular clouds), the escape velocity is still higher than the observed shear velocity. The shear is unlikely to destroy molecular clouds. *The clouds are likely to survive after passing the ridges.*

5. Collision-Induced Star Formation in Bar

The existence of molecular clouds is necessary but not sufficient for star formation (Mooney & Solomon 1988; Scoville & Good 1989; Fukui et al. 1999). There is considerable evidence that cloud-cloud collisions may have initiated star formation (Loren 1976; Scoville, Sanders & Clemens 1986; Odenwald et al. 1992; Hasegawa et al. 1994). The efficiency of collisional dissipation (§4.2) also supports the cloud-based mechanism for triggering star formation. We explore the cloud-cloud collision (or close encounter) model to account for star formation.

5.1. Star Formation at the Leading Side of Ridges

The damping timescale of random motions is close to the rotation timescale $10^8\,\mathrm{yr}$ around the galactic center (§4.2). Thus, the dissipation is not very effective, and newborn stars should follow similar orbits to those of the parent molecular clouds (Figure 9) within about one rotation timescale. Comparing the distribution of the young clusters (Figure 6) to the orbits (Figure 10 *left*), we find that the majority of the clusters are aligned on the outermost orbits in Figure 10. Hence, most star formation occurs at the outer ends of the offset ridges. The same consideration can be applied to other barred galaxies (see Sheth et al. 2002); the outer ends of offset ridges are the primary loci of star formation in bars.

We discussed in §3.4 that some stellar clusters have large offsets from the gas ridges (Figure 6). Considering the isochrons along the orbits (Figure 12) and the clusters' young age $\lesssim 10^7\,\mathrm{yr}$, they should have been born long ($10^7\,\mathrm{yr}$) after the parent clouds passing across the ridges. Star formation is, therefore, triggered even after (but not before) the offset ridges. This cannot be explained by the star formation induced by galactic shocks. In Figure 9 *left*, the separation between orbits is remarkably narrow at the leading side of the ridges. The number density of clouds would therefore be larger at the leading side, and possibly result in more frequent cloud collisions (or close encounters). The collision model explains the star formation after the ridges.

—— Figure 12 ——

The HII regions at the leading side has been a problem for a hydrodynamic model (Sheth et al. 2002). It predicts that the gas looses the tangential velocity at offset shocks, and falls toward the galactic center along the offset ridges (Regan, Sheth & Vogel 1999, see their Figure 9). If star formation occurs due to the shocks, i.e. after the tangential velocity is damped, the newborn stars should also fall *along* the offset ridges and cannot exist at their leading side (Sheth et al. 2002). The orbit model, however, naturally explain the co-motion of molecular clouds and stars, and the star forming regions at the leading side.

Young stars are bright in UV emission for $10^8\,\mathrm{yr}$ after the birth (Iglesias-Paramo, et al 2004), which is close to the rotation timescale. If the young stars follow the gas orbits for a single rotation timescale and if the outer edges of the ridges are the primary loci of star formation, the outermost orbits in Figure 10 *left* would stand out in UV emission from young stars. This is exactly the case for NGC 4303 in the GALEX/UV image (Boissier, in private communication).

5.2. Star Formation at the Bar Ends

Star formation is predominantly found at the outermost radii of the gas ridges in NGC 4303. This is explained by considering the rotation timescale around the galaxy in the rotating frame of the bar. The timescale of passage across the ridges is $\propto 1/(\Omega(r) - \Omega_{\rm b})$, where Ω is the angular rotation speed and the $\Omega_{\rm b}$ is the bar pattern speed. If the rotation velocity is constant, the Ω is the decreasing function $\propto 1/r$ of the galactcentric radius r, and becomes equal to $\Omega_{\rm b}$ at the corotation radius, which is generally close to the bar end and the outermost radii of the ridges. Thus, the molecular clouds at the outermost radii spend more time in the ridges than the ones at inner radii. This

increases the frequency of cloud collisions (or close encounters) at the bar ends and would result in the observed star formation.

6. Conclusions

We observed the central 5 kpc of the barred galaxy NGC 4303 in the CO(1-0) line with the Nobeyama Millimeter Array. We discussed the gas distribution and dynamics, and compared them with young stellar cluster distribution in *HST* images. Main conclusions are summarized:

1. NGC 4303 has the central gas concentration (disk) and offset ridges along its stellar bar. The central disk follows pure circular rotation with slight perturbations due to spiral arms on the disk. Sharp velocity gradients are observed across the offset ridges.

2. Brightness temperature in the resolution ($2.5''$) is much lower than the typical excitation temperature of molecular gas in the Galaxy. Assuming the gas is optically thick in CO(1-0), the beam filling factor is about 0.1, indicating the existence of dense molecular clouds ($\sim 1000 M_\odot$ pc^{-2}) in the offset ridges.

3. The velocity gradient across the offset ridges is about $0.13\,\mathrm{km\,s^{-1}}$ pc^{-1}. This is an order of magnitude smaller than the gradient necessary to break up existing molecular clouds. The clouds survive after passing the offset ridges.

4. Star formation is inactive in Hα image, but a few hundreds of young stellar clusters are found in *HST* images. They have ages $\lesssim 10^7$ yr and masses $10^{3-4} M_\odot$. If the star formation efficiency is 0.01-0.1, their parent molecular clouds should have masses $10^{4-6} M_\odot$.

5. The young clusters are distributed predominantly at the downstream side of the offset ridges. Some of them are located far from the offset ridges, and therefore, they are born after their parent clouds pass the ridges.

6. We used a cloud orbit model to understand the gas dynamics. The dynamics due to slightly-collisional clouds reproduces the central gas disk, narrow offset ridges, and their associated velocity structure. The offset ridges are not necessarily associated with shock.

7. The strength of viscous (damping) force is a parameter of choice in the cloud orbit model. The best fit value gives the timescale 5×10^7 yr for the decay of random motions, which is close to the timescale of cloud-cloud collision or close interaction in NGC 4303.

8. Cloud collision naturally explains the formation of the young clusters far from the offset ridges. Cloud-orbits are densely populated at the leading side of the ridges, indicating high collision frequency and star formation.

We explored a discrete cloud model for understanding the gas dynamics and star formation in NGC 4303. If discrete gas clouds, instead of diffuse hydrodynamic gas, are dominant in gas dynamics, the efficiency of gas fueling to galactic centers would change from the values derived with hydrodynamic simulations. Obviously, there is diffuse, presumably continuous, gas around the discrete clouds. The gas is cycling between the two due to cloud formation, stellar feedback, and ram pressure stripping of cloud envelope, etc. These interplays between diffuse gas and clouds would affect the gas dynamics. To discuss this effect, molecular clouds must be resolved in extragalaxies with higher resolution observations (e. g. ALMA) and simulations (e. g. Wada & Koda 2001).

Appendix 1. Color Evolution of Stellar Cluster

Figure 13 shows the model color evolution of stellar cluster. Three photometric synthesis models are compared, i. e. Bruzual & Charlot 1993 (hereafter, BC93), Fioc & Rocca-Volmerange (Pegase), and Leitherer et al. 1999 (Starburst99). We used the Salpeter initial mass function (IMF) with the mass range $0.1 - 100 M_\odot$ for BC93, the Scalo98 IMF with the range $0.1 - 120 M_\odot$ for Pegase, and the IMF having the indices of 1.3 for $0.1 - 0.5 M_\odot$ and 2.3 for $0.5 - 100 M_\odot$ for Starburst99. The F450W-F814W color drop sharply around 7×10^6 yr for all three models. Perhaps, the uncertainties are a factor of 2 in time and 0.1 mag in magnitude. The stellar clusters bluer than +0.0 mag (§3.3) are, therefore, younger than $\lesssim 10^7$ yr (and 2×10^7 yr at the oldest).

—— Figure 13 ——

We thank Tsutomu Takamiya, Kotaro Kohno, Makoto Hidaka, Hiroyuki Nakanishi, and Sachiko Onodera for useful discussions and collaborations in the Virgo CO survey project. We also thank the NMA staff for their help with observations, Keiichi Wada for fruitful discussions, Ryo Kandori and Samuel Boissier for helping data analysis. We thank Eva Schinnerer for providing her CO data. J. K. was financially supported by the Japan Society for the Promotion of Science for Young Scientists. This work was partially supported by National Science Foundation under grant AST-9981546.

References

Binney, J. & Tremeine, S. 1987, Galactic Dynamics, Princeton University Press
Bruzual, A. G. & Charlot, S. 1993, ApJ, 405, 438
Cardelli, J. A., Clayton, G. C., Mathis, J. S. 1989, ApJ, 345, 245
Colina, L., Garcia Vargas, M. L., Mas-Hesse, J. M., Alberdi, A. & Krabbe, A. 1997, ApJL, 484, 41
Colina, L. & Arribas, S. 1999, ApJ, 514, 637
Colina, L. & Wada, K. 2000, ApJ, 529, 845
Colina, L., Gonzalez Delgado, R., Miguel Mas-Hesse, J., & Leitherer C. 2002, ApJ, 579, 545
Contopoulos, G. & Papayannopoulos, T. 1980, A&A, 92, 33
Dame, T. M., Hartmann, D. & Thaddeus, P. 2001, ApJ, 547, 792
Downes, D., Reynaud, D., Solomon, P. M. & Radford, S. J. E. 1996, ApJ, 461, 186
Ferrarese, L. et al. 1996, ApJ, 464, 568
Fioc, M. & Volmerange, B. 1997, A&A, 326, 950
Fukui, Y., Mizuno, N., Yamaguchi, R., Mizuno, A., Onishi, T., Ogawa, H. et al. 1999, PASJ, 51, 745
Garcia-Barreto, J. A., Franco, J., Carrillo, R., Venegas, S. & Escalante-Ramirez, B. 1996, RMxAA, 32, 89
Hasegawa, T., Sato, F., Whiteoak, J. B., & Miyawaki, R. 1994, ApJ, 429, 77
Helfer, T. T., Thornley, M. D., Regan, M. W., Wong, T., Sheth, K., Vogel, S. N., Blitz, L. & Bock, D. C. -J. 2003, ApJS, 145, 259
Ho, L. C., Filippenko, A. V., & Sargent, W. L. W. 1997, ApJS, 112, 315
Iglesias-Paramo, J., Boselli, A., Gavazzi, G., Zaccardo, A. 2004, A&A, 421, 887
Ishizuki, S., Kawabe, R., Ishiguro, M., Okumura, S. K., Morita, K. -I. 1990, Nature, 344, 224
Jimenez-Bailon, E., Santos-Lleo, M., Mas-Hesse, J. M., Guainazzi, M., Colina, L., Cervino, M. & Gonzalez Delgado, R. M. 2003, ApJ, 593, 127
Kenney, J. D. & Young, J. S. 1988, ApJS, 66, 261
Koda, J., Sofue, Y., Kohno, K., Nakanishi, H., Onodera, S., Okumura, S. K., Irwin, J. A.
Koda, J. & Wada, K. 2002, A&A, 396, 867
Koopmann, R. A., Kenney, J. D. & Young, J. 2001, ApJS, 135, 125
Lada, E. A. 1992, ApJL, 393, 25
Leitherer, C., Schaerer, D., Goldader, J. D., Dalgado, R. M. G. et al. 1999, ApJS, 123, 3
Loren, R. B. 1976, ApJ, 209, 446
Moellenhoff, C. & Heidt, J. 2001, å, 368, 16
Mooney, T. J. & Solomon, P. M. 1988, ApJ, 334, 51
Nakanishi, H., Sofue, Y. & Koda, J. 2005, PASJaccepted
Nishiyama, K. & Nakai, N. 2001, PASJ, 53, 713
Odenwald, S., Fischer, J., Lockman, F. J., & Stemwedel, S. 1992, ApJ, 397, 174
Oka, T., Hasegawa, T., Sato, F., et al. 2001, ApJ, 562, 348
Okumura, S. K., et al. 2000, PASJ, 52, 393
Onodera, S., Koda, J., Sofue, Y. & Kohno, K. submitted to PASJ
Regan, M. W., Teuben, P. J. & Vogel, S. N. 1996, AJ, 112, 6
Regan, M. W., Sheth, K. & Vogel, S. N. 1999, ApJ, 526, 97
Regan, M. W. & Teuben, P. J. 2004, ApJ, 600, 595
Reynaud, D. & Downes, D. 1998, A&A, 337, 671
Sakamoto, K., Okumura, S. K., Ishizuki, S. & Scoville, N. Z. 1999, ApJS, 124, 403
Sakamoto, K, Baker, A. J. & Scoville, N. Z. 2000, ApJ, 533, 149
Schinnerer, E., Maciejewski, W., Scoville, N., Moustakas, L. A. 2002, ApJ, 575, 826
Scoville, N. Z. & Good, J. C., 1989, ApJ, 339, 149
Scoville, N. Z., Sanders, D. B., & Clemens, D. P. 1986, ApJ, 310, 77
Scoville, N. Z. & Sanders, D. B. 1987, Interstellar Process, ed. D. Hollenbach and H. Thronson (Durdrecht: Reidel).
Sheth, K., Regan, M. W., Vogel, S. N., & Teuben, P. J. 2000, ApJ, 531, 221
Sheth, K., Vogel, S. N., Regan, M. W., Teuben, P. J., Harris, A. I., & Thornley, M. D. 2002, AJ, 124, 2581
Sofue, Y., Koda, J., Nakanishi, H., Onodera, S., Kohno, K., Tomita, A. & Okumura, S. K. 2003, PASJ, 55, 17
Sofue, Y., Koda, J., Nakanishi, H. & Onodera, S. 2003, PASJ, 55, 59
Sofue, Y., Koda, J., Nakanishi, H. & Hidaka, M. 2003, PASJ, 55, 75
Solomon, P. M., Rivolo, A. R., Barrett, J., & Yahil, A. 1987, ApJ, 319, 730
Wada, K. 1994, PASJ, 46, 165
Wada, K. & Koda, J. 2001, PASJ, 53, 1163
Zacharias, N., et al. 2000, AJ, 120, 2131
Combes, F. 1996, in ASP Conf. Ser. 91, Barred Galaxies, ed. R. Buta, D. A. Crocker & B. G. Elmegreen (San Francisco; ASP), 286
Evans, N. J. & Lada, E. A. 1991, in IAU Symposium 147, Fragmentation of Molecular Clouds and Star Formation, ed. E. Falgarone & Duvert (Durdrecht: Kluwer)
Scoville, N. Z. & Sanders, D. B. 1987, in Interstellar Process, ed. D. Hollenbach and H. Thronson (Durdrecht: Reidel).
Tsutumi, T., Morita, K. -I., & Umeyama, S. 1997, in ASP Conf. Ser. 125, Astronomical Data Analysis Software and Systems VI, ed. G. Hunt & H. E. Payne (San Francisco; ASP), 50
de Vaucouleurs, G., de Vaucouleurs, A. Corwin, H. G., Buta, R. J., Paturel, G., & Fouque, P. 1991, Third Reference Catalogue of Bright Galaxies (Berlin: Springer)

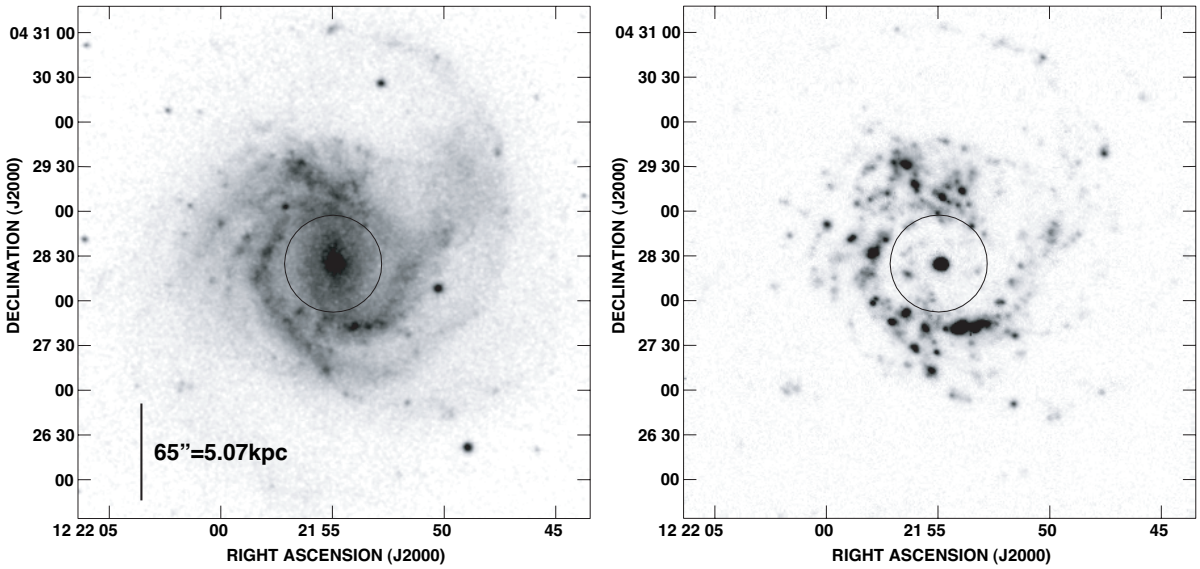

Fig. 1. *Left:* B-band image of NGC 4303 from the Digitalized Sky Survey. *Right:* Hα image from Koopmann, Kenney & Young (2001). Circles represent the primary beam size of the ^{12}CO(J = 1 − 0) observations (65″ HPBW).

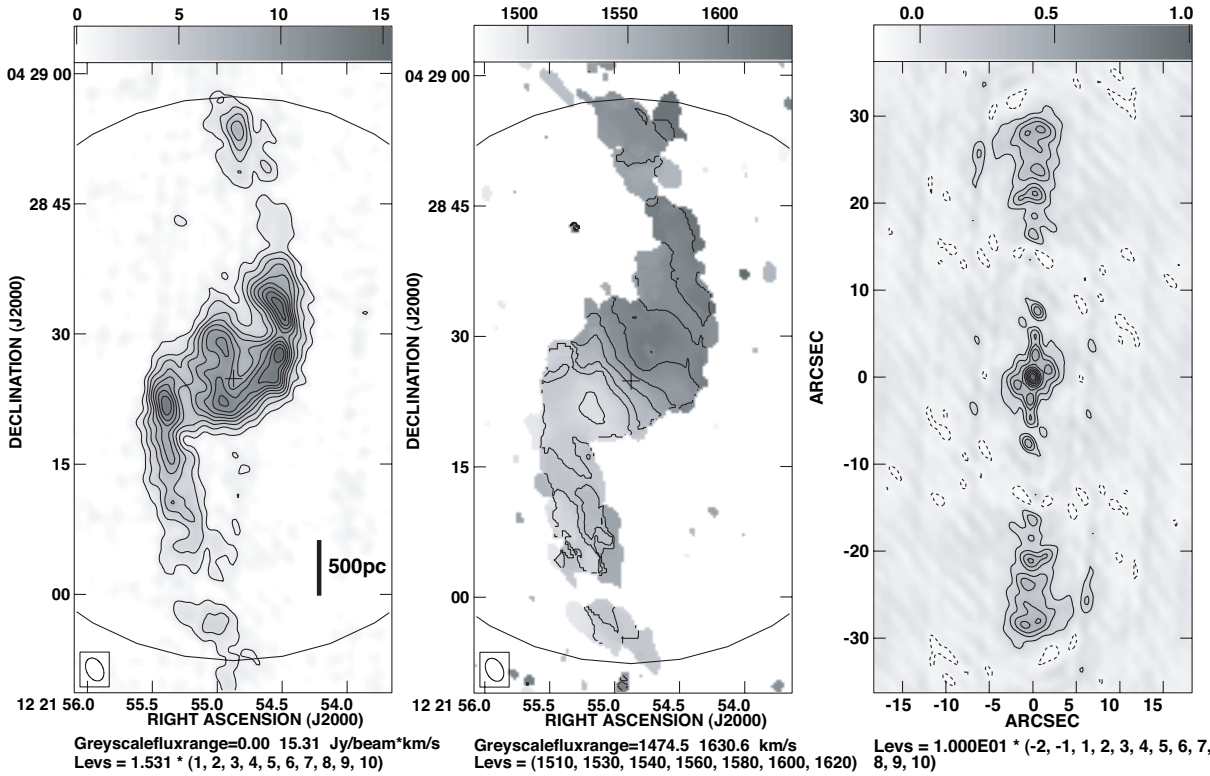

Fig. 2. CO(1-0) zeroth- and first-moment maps of NGC 4303, and synthesized beam map. A clip at the 2σ level was used to make these maps. Circles represent the primary beam size of observations. No primary beam correction has been applied.

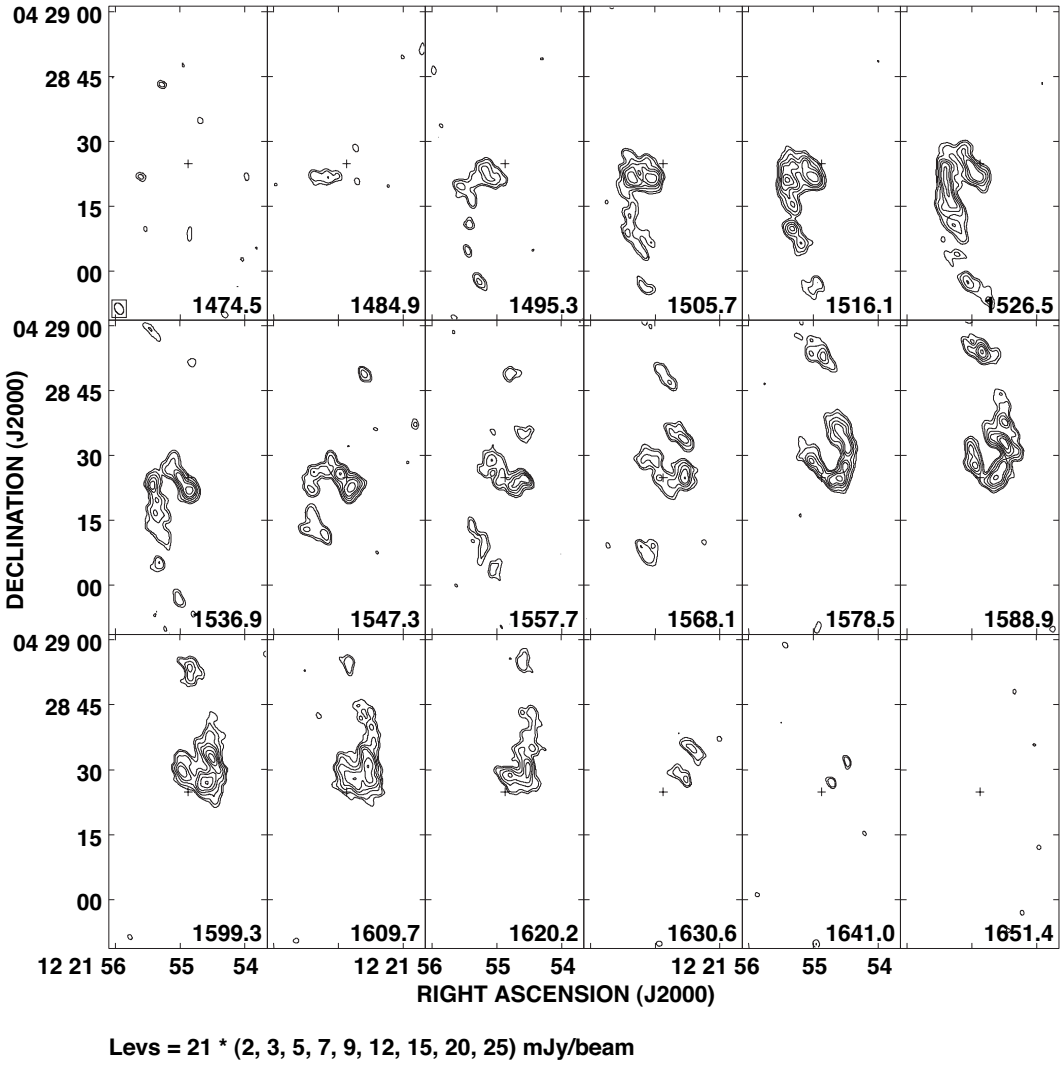

Fig. 3. CO(1-0) velocity channel maps of NGC 4303 in the same region as in Figure 2. Velocities at the channels are shown at the lower right corners. No primary beam correction has been applied. The $1\,\mathrm{mJy\,beam^{-1}}$ corresponds to 0.017K in brightness temperature.

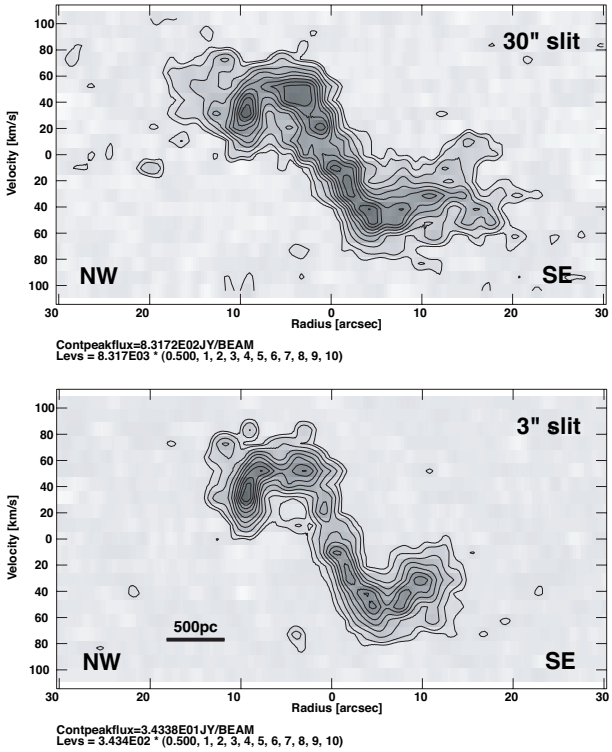

Fig. 4. Position-velocity diagrams with PA $= -44.45$ and slit widths of $30''$ (*upper panel*) and $3''$ (*lower panel*). Contours are 0.05, 0.1, 0.2, 0.3, 0.4, 0.5, 0.6, 0.7, 0.8, 0.9, 1.0 times the peak intensity.

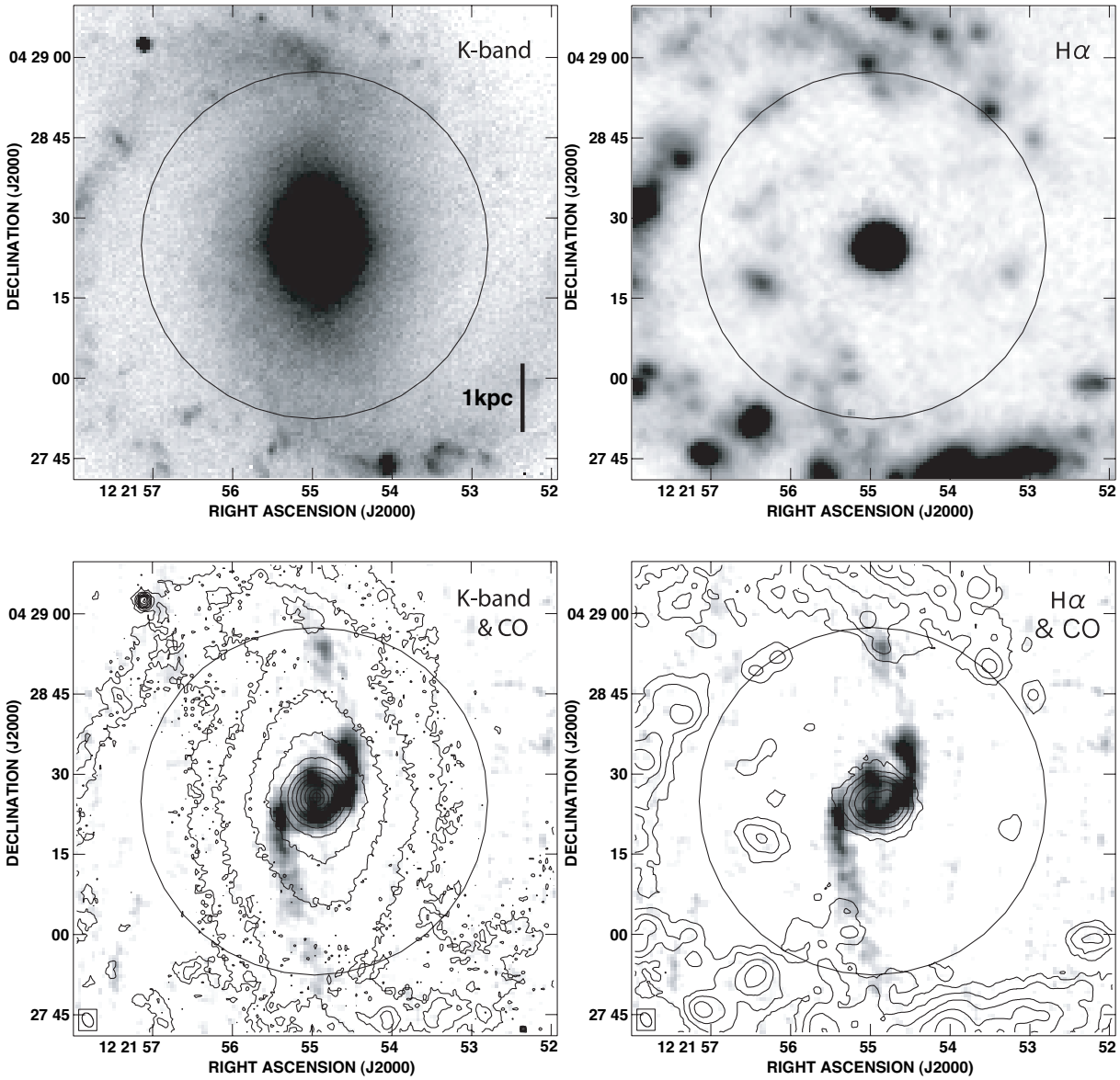

Fig. 5. K-band and Hα images of the central $90'' \times 90''$ region of NGC 4303. *Upper-left:* K-band image. *Lower-left:* K-band contours on CO greyscale image. Contours are 0.008, 0.012, 0.018, 0.027, 0.041, 0.061, 0.091, 0.14, 0.21, 0.31, 0.46, 0.69, 1.0 times the peak K-band intensity. *Upper-right:* Hα image. *Lower-right:* Hα contours on CO greyscale image. Contours are 0.031, 0.063, 0.125, 0.25, 0.5, 1.0 times the peak Hα intensity. Circles represent the field-of-view (FWHM) of CO observations.

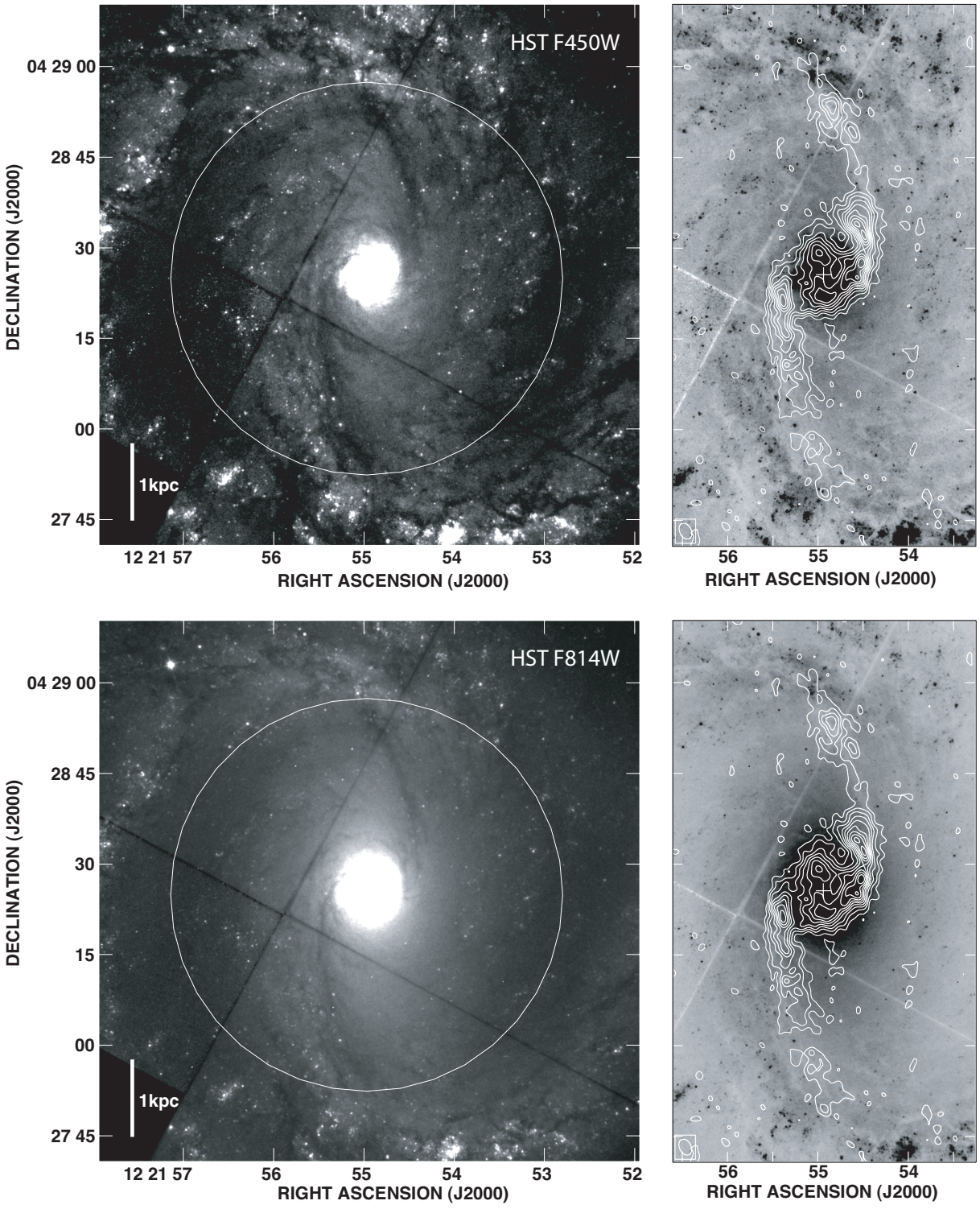

Fig. 6. HST images of the central $90'' \times 90''$ region of NGC 4303, the same region covered in Figure 1. *Upper panels:* HST F450W band images. *Lower panels:* HST F814W band images. Right panels are the central vertical strips of the left images, and CO contours are overlayed on HST greyscale images. Contours are 0.1, 0.2, 0.3, 0.4, 0.5, 0.6, 0.7, 0.8, 0.9, 1.0 times the peak CO intensity. Circles represent the FoV (FWHM) of CO observation.

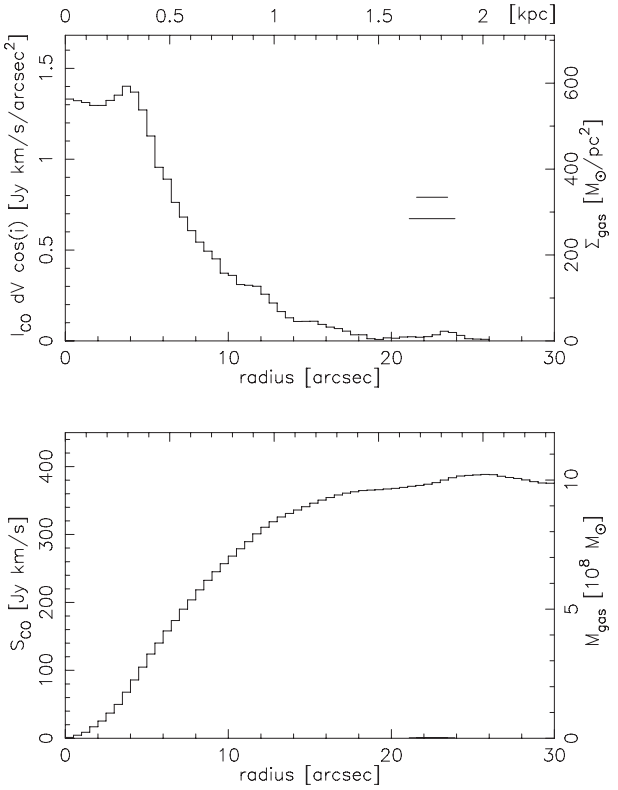

Fig. 7. Radial profiles of integrated-intensity (inclination corrected). Physical scales at the top and right axes are calculated by using the distance of 16.1 Mpc and conversion factor of $X_{\rm CO} = 1.8 \times 10^{20}\,{\rm cm}^{-2}[{\rm K\,km\,s}^{-1}]^{-1}$. We assumed $M_{\rm gas} = 1.41 M_{\rm H_2}$, taking He and other elements into account. Two horizontal lines indicate the sizes of major and minor axes of the synthesized beam.

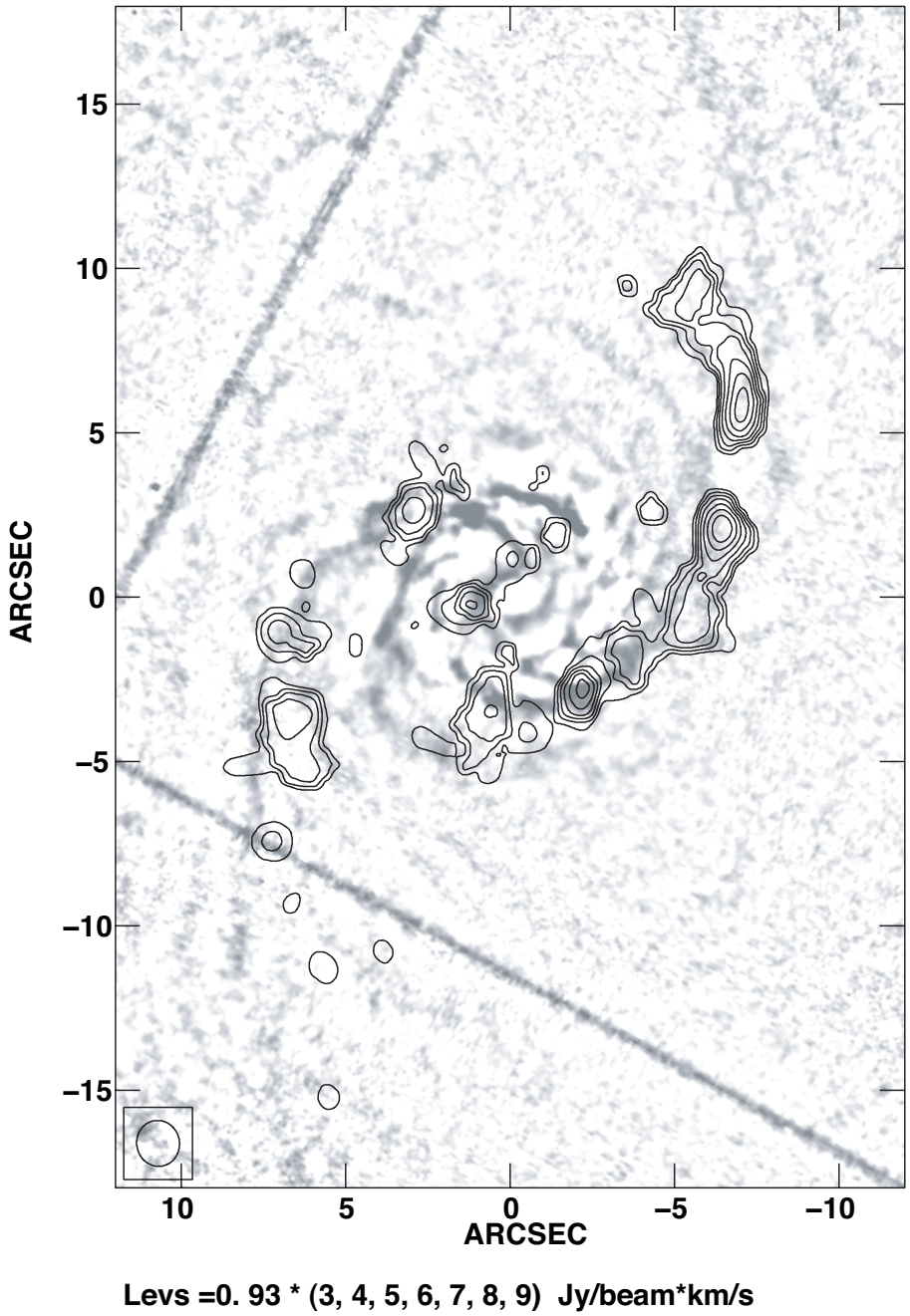

Fig. 8. High resolution (uniform weighting) CO contours at the top of an unsharp-masked *HST* F814W image. Contours are 0.3, 0.4, 0.5, 0.6, 0.7, 0.8, 0.9 times the peak intensity 0.9 Jy/beam*km/s.

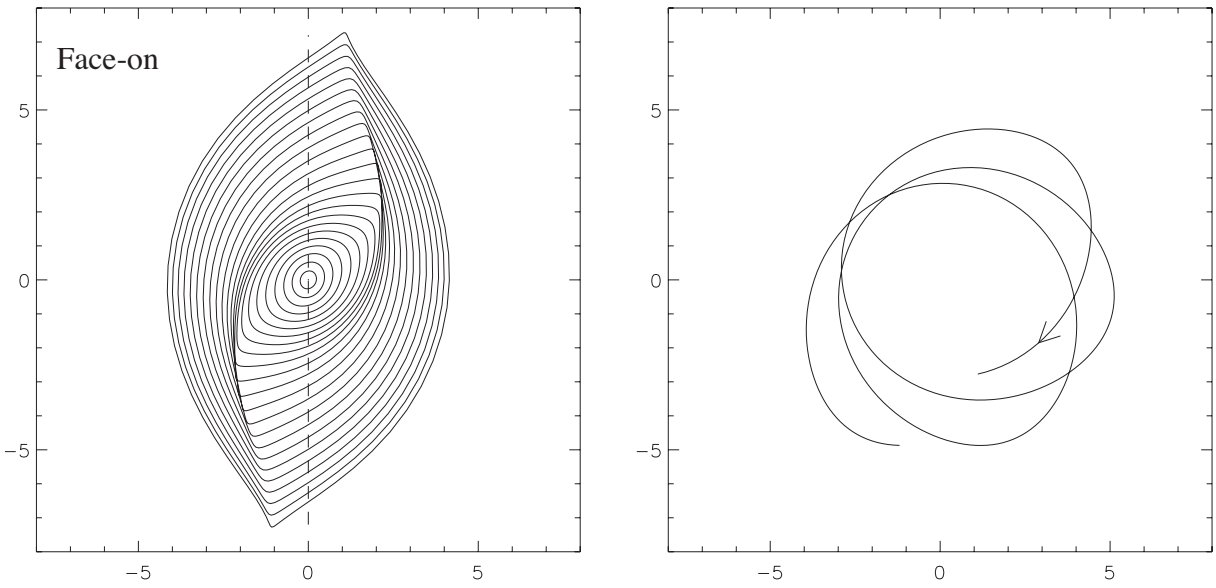

Fig. 9. *Left:* Gas orbits in a bar in the rotating frame with the bar (clockwise rotation). Dashed line indicates the bar direction. *Right:* An orbit in the non-rotating reference frame. The gas is rotating clockwise in both panels. We used the potential $\Phi(R,\varphi) = (1-\epsilon\cos 2\varphi)\frac{v_0^2}{2}\log(1+(R/a)^2)$ where $a=1$, $v_0=1$ and $\epsilon=0.04$. Pattern speed of the bar is $\Omega_\mathrm{b}=0.1$. The two inner Lindblad resonances and corotation radii are $R_\mathrm{ILR}=1.1, 2.0$, and $R_\mathrm{CR}=9.9$, respectively. Assuming the bar length of 6 kpc ($77''$) and rotational velocity of $160\,\mathrm{km\,s^{-1}}$ at the radius of 3 kpc, the units of the model become $a=300\,\mathrm{pc}$ ($3.8''$), $v_0=160\,\mathrm{km\,s^{-1}}$, and $\Omega_\mathrm{b}=53\,\mathrm{km\,s^{-1}\,kpc^{-1}}$.

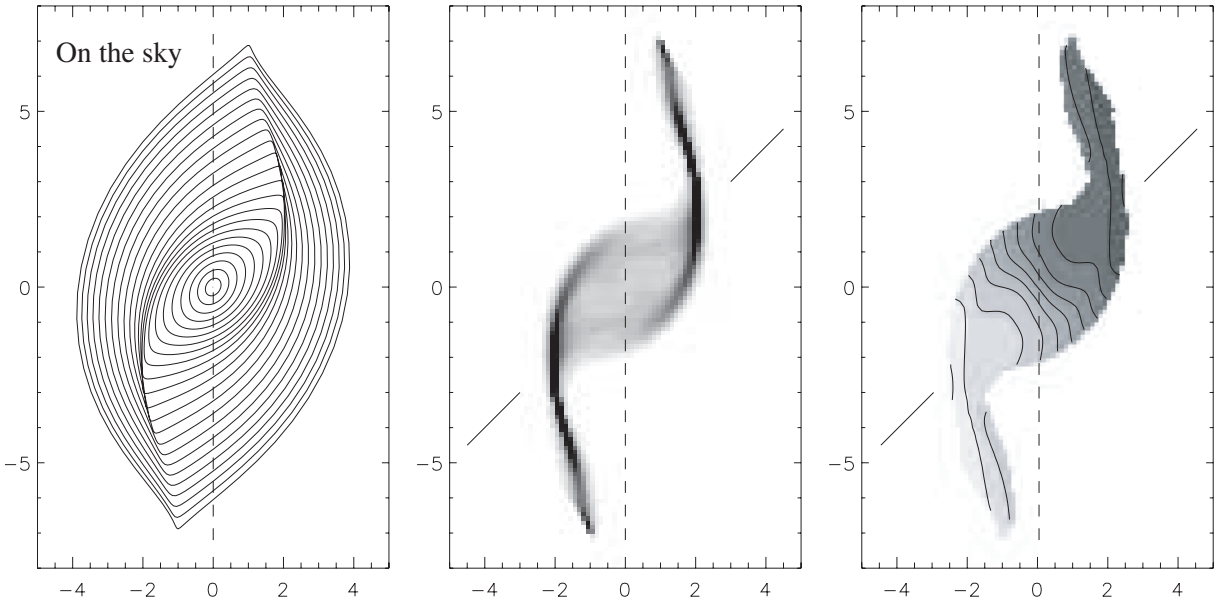

Fig. 10. *Left:* Gas orbits in a bar projected on the sky. Position angle and inclination are $-45°$ and $30°$, respectively. We first rotated the gas orbits (Figure 9 *left*) counterclockwise by $4°$, so that the bar (dashed line) runs vertically as that in NGC 4303. *Middle:* Density map. This is calculated from the gas orbits based on the speed of gas motions. Radial density profile is set to be $\exp(-r/4)$ in $r > 2$ and constant in $r \leq 2$. We cut low density region with an arbitrary threshold. Solid lines indicate the major axis (P.A. $= -45°$). *Right:* Velocity field, calculated from the gas orbit model.

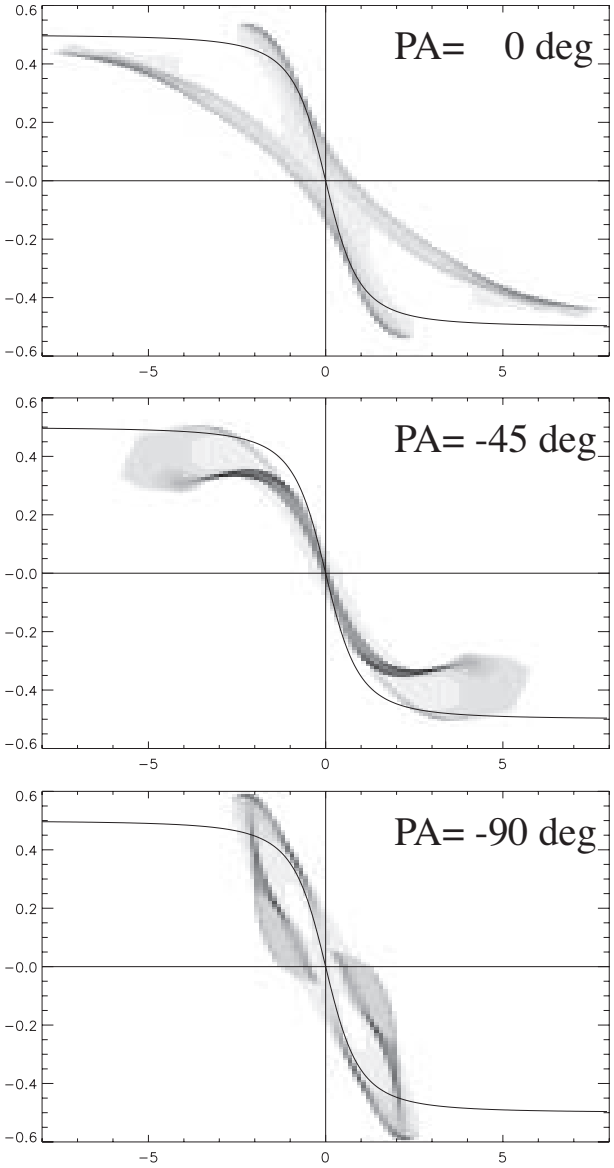

Fig. 11. Position-velocity diagrams of the model in Figure 10 observed from three different angles. The position angles of the galaxy major axis are 0° (*top*), −45° (*middle*), and −90° (*bottom*). Solid curves are the rotation curve given by the assumed potential.

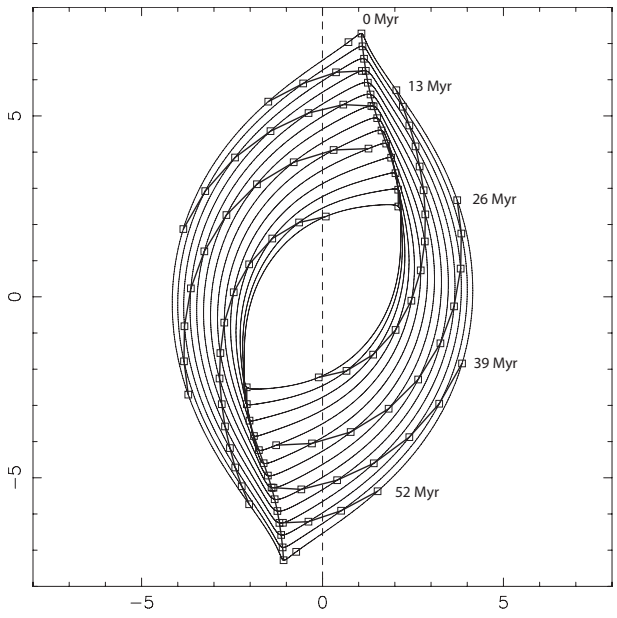

Fig. 12. Isochrones of gas flows. Thick solid lines indicate 0, 13, 26, 39, 52 Myr after the passage of turning points (offset ridges). Gas orbits (same as Figure 9) are also shown for reference.

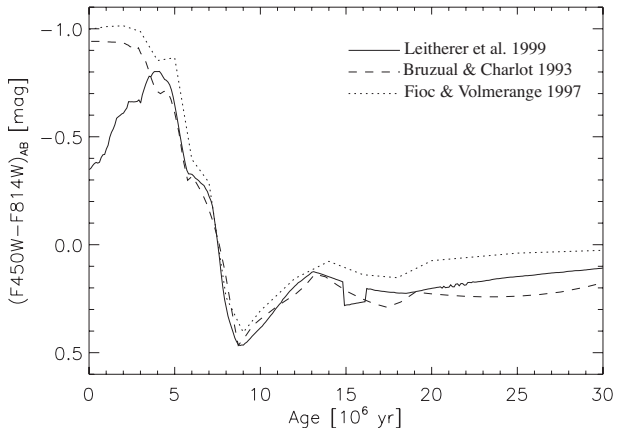

Fig. 13. Model color evolution of stellar cluster.

Table 1. Parameters of NGC 4303

Parameter	Value	Reference
Alias	M61	
Hubble type	SAB(rs)bc	1
Nuclear activity	H	2
Distance (Mpc)	16.1	3
Linear scale of $1''$ (pc)	78.1	
P.A.(isophotal)		
Inclination (isophotal)		
$V_{\rm sys}$ ($\rm km\,s^{-1}$)	1569	1
D^0_{25} (arcmin)	6.46	1
B^0_T (mag)	10.12	1
$S_{CO(1-0)}(45'')$ ($\rm Jy\,km\,s^{-1}$)	494 ± 87	4
$S_{CO(1-0)}(13'')$ ($\rm Jy\,km\,s^{-1}$)	193 ± 6	5

References: (1) de Vaucouleurs, G. et al. 1991; (2) Ho, Filippenko & Sargent 1997; (3) Ferrarese et al. 1996; (4) Kenney & Young 1988, $45''$ (FHWM) beam centered at $\alpha_{1950} = 12^{\rm h}19^{\rm m}21^{\rm s}.4$ and $\delta_{1950} = +4^\circ44'58''.0$; (5) Nishiyama & Nakai 2001, $16''$ (FHWM) beam centered at $\alpha_{1950} = 12^{\rm h}19^{\rm m}21^{\rm s}.4$ and $\delta_{1950} = +4^\circ44'58''.0$

Table 2. Observational Parameters

Parameter	Value
Year	1999 Dec. - 2000 Feb.
Field Center	
α_{1950}, δ_{1950}	$12^{\rm h}19^{\rm m}21^{\rm s}.60$, $+4^\circ45'03''.0$
α_{2000}, δ_{2000}	$12^{\rm h}21^{\rm m}54^{\rm s}.97$, $+4^\circ28'24''.9$
Field of View	$65''$
Array Configuration	AB, C, D
Observing Frequency	114.65925 GHz
Band width	512 MHz

Table 3. Parameters of CO(1-0) Cube

Parameter	Value	Value
Configuration	AB+C+D	AB+C+D
Weighting	NA	UN
Synthesized Beam	$2.8'' \times 1.9''$,166°	$1.4'' \times 1.3''$,11°
ΔV ($\mathrm{km\,s^{-1}}$)	10.4	31.2
rms ($\mathrm{mJy\,beam^{-1}}$)	21	24
T_b for $1\,\mathrm{Jy\,beam^{-1}}$	17.3	50.5
T_b for $1\,\mathrm{Jy\,arcsec^{-2}}$	91.9	91.9

Table 4. Kinematic Parameters of The Nuclear Disk

Parameter	Value
Dynamical Center	
α_{1950}, δ_{1950}	$12^{\mathrm{h}}19^{\mathrm{m}}21^{\mathrm{s}}.67$, $+4°45'03''.7$
α_{2000}, δ_{2000}	$12^{\mathrm{h}}21^{\mathrm{m}}54^{\mathrm{s}}.94$, $+4°28'25''.6$
V_{sys} ($\mathrm{km\,s^{-1}}$)	1556.5
P.A. (deg)	-44.45
i (deg)	29.13